Supporting Information

Rapid Solidification for Green-Solvent-Processed Large-Area Organic Solar Modules with >16% Efficiency

Ben Zhang,[a] Weijie Chen,[a] Haiyang Chen,[a] Guang Zeng,[a] Rui Zhang,[d] Hongxiang Li,[e] Yunfei Wang,[f] Xiaodan Gu,[f] Weiwei Sun,[a] Hao Gu,[a] Feng Gao,[d] Yaowen Li,[a,b,c]* and Yongfang Li[a,b,g]

[a] Laboratory of Advanced Optoelectronic Materials, Suzhou Key Laboratory of Novel Semiconductor-optoelectronics Materials and Devices, College of Chemistry, Chemical Engineering and Materials Science, Soochow University, Suzhou 215123, China
Email: ywli@suda.edu.cn

[b] Jiangsu Key Laboratory of Advanced Negative Carbon Technologies, Soochow University, Suzhou 215123, China

[c] State and Local Joint Engineering Laboratory for Novel Functional Polymeric Materials, Jiangsu Key Laboratory of Advanced Functional Polymer Design and Application, College of Chemistry, Chemical Engineering and Materials Science, Soochow University, Suzhou 215123, China

[d] Department of Physics, Chemistry and Biology (IFM), Linköping University, Linköping SE-58183, Sweden

[e] College of Polymer Science and Engineering, State Key Laboratory of Polymer Materials Engineering, Sichuan University, Chengdu 610065, China

[f] School of Polymer Science and Engineering, Center for Optoelectronic Materials and Devices, The University of Southern Mississippi, Hattiesburg, Mississippi 39406, United States

[g] Beijing National Laboratory for Molecular Sciences; CAS Key Laboratory of Organic Solids, Institute of Chemistry, Chinese Academy of Sciences, Beijing 100190, China

Experimental Section

1. Materials

Indium-tin-oxide (ITO) glass was purchased from South China Xiang Science and Technology Company Ltd. Zinc acetate dihydrate ($Zn(CH_3COO)_2•2H_2O$, 98%) was purchased from Sigma-Aldrich. Aluminum nitrate ($Al(NO_3)_3•9H_2O$, 99.99%) and ethylene glycol (EG, 99%) were purchased from Aladdin. Toluene (PhMe), *o*-xylene (*o*-XY), and 1,2,4-trimethyl-benzene were purchased from J&K Scientific. PEDOT:PSS (Heraeus Clevios PVPA 4083) was purchased from Heraeus. The polymer donor PM6, D18 and non-fullerene acceptor L8-BO were purchased from Solarmer materials Ltd. All of the materials were used as received without further purification.

2. Device fabrication

Small-area device fabrication: The OSCs were fabricated with an inverted structure of ITO/AZO/Active layer/MoO_3/Al. ITO-coated glass substrates were rinsed with deionized water, acetone, and isopropyl alcohol by ultrasonication, sequentially, and then dried with N_2. After that, the AZO layer was blade-coated on top of ITO substrate with a coating velocity of 10 mm/s and gap height of 200 μm in the air and then dried at 140°C for 20 min. The active layer solution was prepared with PM6:D18:L8-BO ratios of 0.8:0.2:1.2 (w/w, 5.6 mg/mL of PM6) in PhMe with 1,4-diiodobenzene (DIB) as a solid additive (the content of DIB is 50% of the total mass of donor and acceptor). Then the active layer solution was stirred at 80°C for 6 hours to ensure complete dissolution, followed by stirring at 25°C for 2 hours. Subsequently, the PM6:D18:L8-BO blend film was blade-coated in the ambient atmosphere onto the AZO layer at a blade-coated speed of 7 mm/s, and thermally annealed at 85°C for 5 min. For RS processing, the blend film is immediately dried by N_2 after the blade-coating. Finally, a MoO_3 layer (10 nm) and an Al film (100 nm) were thermally deposited on the active layer by vacuum evaporation under 3×10^{-4} Pa.

Large-area (5×5 cm^2) module fabrication: The module was fabricated with a similar device architecture to the small-area OSCs. The series interconnection of the module was realized by P1, P2, and P3 lines, which were patterned using a laser etching system

with a GH-LS300. The gap between each ITO pattern is defined as P1 with a width of 30 μm. The patterned ITO-coated glass substrates (5×5 cm^2) were rinsed, which was followed by depositing the AZO, active layer, and MoO_3 layer were fabricated as depicted before. Then the organic layers were partially removed by high-resolution short-pulse laser for subsequent serial interconnection of the individual cell (the width of P2 line is around 140 μm). Finally, an Al electrode (100 nm) was deposited on MoO_3 layer by vacuum evaporation and the P3 (80 μm) line was formed to complete the module and make the Al to ITO interconnection between adjacent cells.

Large-area (10×10 cm^2) module fabrication: The 10×10 cm^2 module was fabricated using the same device process to the 5×5 cm^2 OSC module, which consists of sixteen sub-cells (9.0×0.5 cm^2) monolithically in series. The width of dead area is 0.42 μm, and the geometric fill factor of module is about 92.2%.

3. Electrical measurements

The *J–V* characteristics of the devices were measured with a computer-controlled Keithley 2400 Source Measure Unit under AM 1.5G illumination (100 mW cm^{-2}) from a SS-F5-3A solar simulator (Enli Technology). The light intensity was calibrated by a standard silicon solar cell (SRC-00178, calibrated by Enli Technology) before testing. The EQE spectra were obtained using a solar cell spectral response measurement system (Enli Technology Co., Ltd., QE-R3011). The light intensity at each wavelength was also calibrated with a standard silicon solar cell (RCS103011-E, calibrated by Enli Technology).

4. UV-visible absorption spectra measurements

The absorption spectra were measured with an ultraviolet spectrometer (Agilent Technologies Cary 5000 UV-vis-NIR).

5. *In-situ* UV-visible absorption spectra measurements

In-situ UV-vis absorption measurements were performed by the Optosky spectrometer using the transmission mode. The minimum integration time was 20 ms with automatic

recoded spectra every 25 ms.

6. LBIC mapping measurements

The LBIC mapping measurements were carried out by using Professional LBIC (InfinityPV ApS). The system was equipped with a 635 nm laser and 2D/3D LBIC image function.

7. Morphology characterization

AFM images were measured on an atomic force microscope (Bruker Nanoscope V) and TEM images were measured on a FEI Tecnal G2 F20.

8. 2D GIWAXS measurements

The samples were prepared on Si substrates using identical conditions with the device fabrication. The 2D GIWAXS measurement was conducted at beamline 7.3.3 at the Advanced Light Source at Lawrence Berkeley National Lab (Berkeley, USA). The samples were illuminated with 10 keV radiation ($\lambda = 1.24$ Å) at an incident angle (αi) of 0.12°. The beam size was 300 μm (height) × 700 μm (width). The scattering signal was captured on a Pilatus 2M (172 μm pixel size, file format EDF, 1475 × 1679 pixels) located 282 mm from the sample. The GIWAXS data in Fig. S8 were obtained at beamline BL02U2 of Shanghai Synchrotron Radiation Facility (SSRF). The monochromatic of the light source was 1.24 Å. The data were recorded by using the two-dimensional image plate detector of Pilatus 2M from Dectris, Switzerland. The crystal coherence length (CCL) was calculated by using the Scherrer equation:

$$CCL = \frac{2\pi K}{\Delta q}$$

Where K is the shape factor (K = 0.9), and Δq is the full-width at half-maximum (FWHM) of the diffraction peak.

9. Stability measurements

Operational stability measurements of the OSCs were conducted by using the white

light LED array under continuous illumination of the simulating intensity of 100 mW cm^{-2} (spectral region: 410-850 nm, Suzhou D & R Instruments, PVLT-G8001M-32B) at MPP (N_2 atmosphere, temperature around 45-55°C) and the currents were recorded over time with the Keithley 2400 source meter.

10. Marangoni number calculation

The Marangoni number (*Ma*) was used to evaluate the strength of the Marangoni effect. The surface tension values of the PM6:D18:L8-BO films were determined via contact angle measurement. ΔT is calculated by the temperature difference between the bottom and top of the wet film, which is determined by subtracting room temperature from different substrate temperatures. The thickness of wet film was calculated from the solution volume (22 μL) and the ITO glass area (1.5×1.5 cm^2).[1] Solution viscosities at different temperatures were measured with a viscometer. The thermal diffusivity $\alpha = k/(\rho C_P)$, where k, ρ, and C_P are thermal conductivity, density, and specific heat capacity of the toluene solvent, respectively. The relevant parameters can be accessed through the National Institute of Standards and Technology (NIST) database at https://webbook.nist.gov/chemistry/fluid/.

11. Electroluminescence quantum efficiency measurements

The electroluminescence quantum efficiency (EQE_{EL}) values were recorded with an electroluminescence measurement system (VLAS, LightSkytech) with a Hamamatsu silicon photodiode 1010B. A Keithley 2400 was used for supplying bias voltages and recording injected current, and a Keithley 485 was used for collecting the photocurrent generated from the emitted photons of the samples.

12. Contact angle measurement and calculation of surface tension

Contact angles were measured on an Attension Theta Optical tensiometer (Biolin Scientific) at room temperature. The surface tension value was calculated according to the following equation:

$\gamma_{LV}(1 + \cos\theta) = 2\sqrt{\gamma_{SV}^{d}\gamma_{LV}^{d}} + 2\sqrt{\gamma_{SV}^{p}\gamma_{LV}^{p}}$, where γ_{SV}^{d} and γ_{LV}^{d} represent the dispersion part of the surface tension between solid-air and liquid-air, respectively. γ_{SV}^{p} and γ_{LV}^{p} represent the polar part of the surface tension between solid-air and liquid-air, respectively. The surface tensions of water and diiodomethane are 72.8 mN m^{-1} (γ_{LV}^{p} = 50.7 mN m^{-1} and γ_{LV}^{d} = 22.1 mN m^{-1}) and 50.8 mN m^{-1} (γ_{LV}^{p} = 6.7 mN m^{-1} and γ_{LV}^{d} = 44.1 mN m^{-1}). And $\gamma_{SV} = \gamma_{SV}^{d} + \gamma_{SV}^{p}$

Supplementary discussion 1: Mechanism related to the direction of surface tension

The fundamental reason for surface tension is the uneven distribution of interaction forces at the gas-liquid interface. Solvent molecules in a liquid are categorized into those residing within the liquid bulk and those at the gas-liquid interface. Molecules within the liquid bulk are subjected to symmetric interaction forces from neighboring solvent molecules, which cancel each other out. However, molecules at the gas-liquid interface are exposed to interaction forces from solvent molecules aimed towards the liquid bulk, as well as from gas molecules directed towards the gas phase. Since the interaction forces from the gas side are much weaker than those from the liquid side,[2] solvent molecules at the gas-liquid interface are subjected to interaction forces directed towards the liquid interior.

Supplementary discussion 2: The calculation of evaporation rate

The value of evaporation rate is obtained by Dalton evaporation empirical formula:

$$\omega = 0.22 \times (E - e) \times \sqrt{1 + 0.32 \times v^2}$$

where ω is the evaporation rate (mm/d), E is the saturated vapor pressure of the solvent (hpa), e is the vapor pressure above the solution (hpa), and v is the airflow velocity (m/s). The saturated vapor pressure of PhMe at 25°C is about 2.67 Kpa, which represents the E value. To simplify the calculation process, the value of e can be approximated as the saturated vapor pressure of PhMe multiplied by the relative humidity (40%, $e = E \times 40\%$). The airflow velocity v can be measured by an anemometer.

Supplementary discussion 3: The reason for using solvent vapor annealing as a post-treatment in verifying the effect of different evaporation rates on molecular crystallization

Thermal annealing (TA) and solvent vapor annealing (SVA) as the most common post-treatment applied in OSCs, which are mainly used to form suitable phase separation and promote molecular crystallization. For TA, the free energy of organic molecules decreases during this process, and the intermolecular assembly will be more orderly,

thus improving the molecular crystallinity. For SVA, the organic molecular is exposed to an environment saturated with solvent vapor that diffuse into the organic molecular, inducing a re-assembly of molecular via strong solvent-molecular interactions. This interactions can promote crystal growth and lead to an increase in crystal size, which is beneficial for amplifying the crystallization distinction under different evaporation rates.

Supplementary discussion 4: The calculation of energy loss

To clarify the origin of increased V_{oc} value in the RS-based device, energy loss (E_{loss}) analysis was performed based on the detailed balance theory. The E_{loss} could be classified into three different constituents ($E_{loss} = E_g - qV_{oc} = \Delta E_1 + \Delta E_2 + \Delta E_3$), where E_g, ΔE_1, ΔE_2 and ΔE_3 denote the optical bandgap, thermodynamic loss, blackbody radiation-induced loss and non-radiative recombination loss, respectively. As presented in Fig. S19, SI, the E_g of the RT-, HT- and RS-based blend films are 1.43, 1.44 and 1.46 eV, respectively, where E_gs were obtained from the derivative of the EQE spectra.[3] The resulting E_{loss} of RS-based device (0.565 eV) is lower than those of the RT- and HT-based devices (0.585 and 0.573 eV, respectively), showing reduced charge recombination loss. Given that all devices showed similar ΔE_1 and ΔE_2 values (Fig. S19 and Table S14, SI), the marked V_{oc} differences primarily arise from ΔE_3.

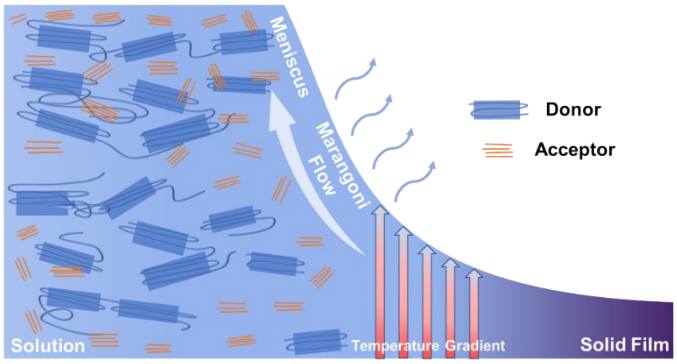

Fig. S1 The schematic illustration of the Marangoni effect at high temperature.

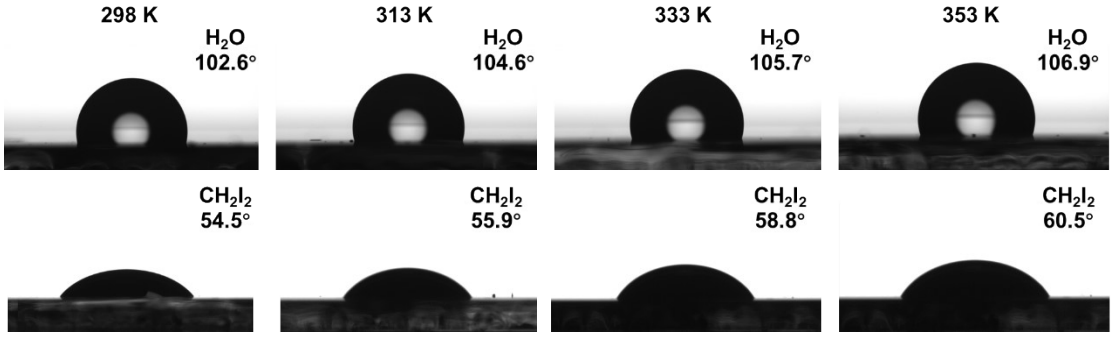

Fig. S2 The images of the water droplet contact angles and diiodomethane droplet contact angles on the surfaces of blend films at different substrate temperatures.

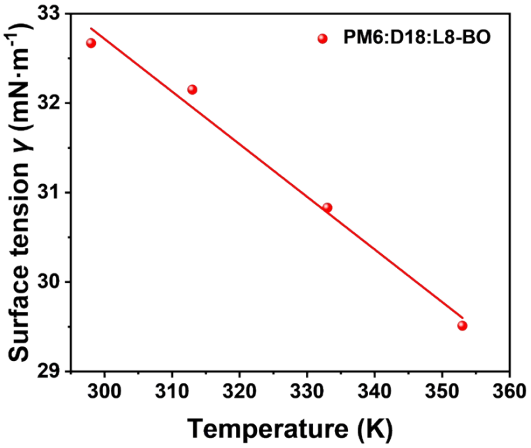

Fig. S3 The surface tension γ versus substrate temperatures by a linear relationship for PM6:D18:L8-BO. The slope of curve is -0.059.

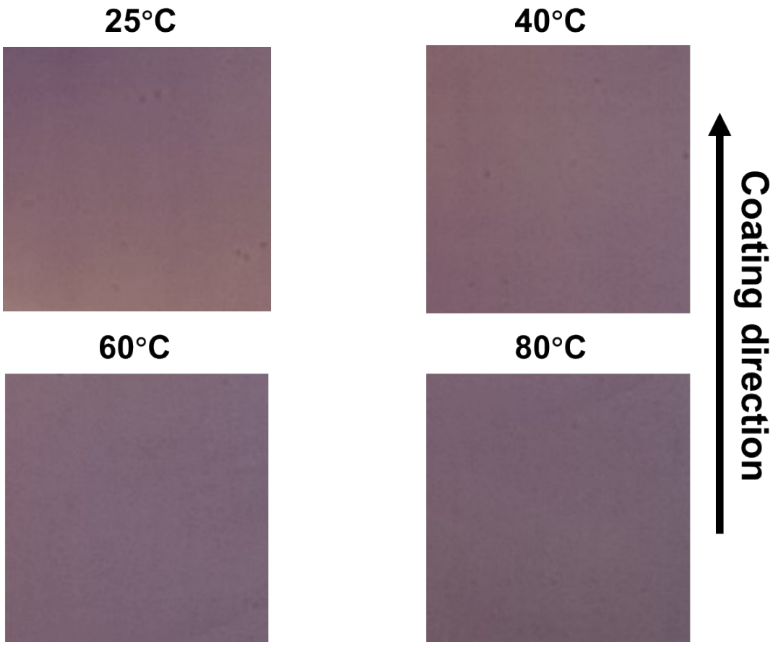

Fig. S4 Photographs of active layer films at different substrate temperatures captured using a digital camera with macro-lens.

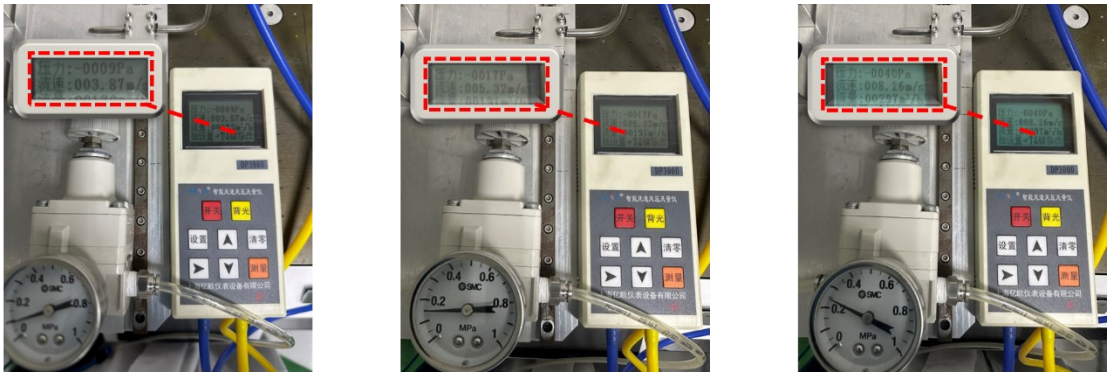

Fig. S5 The measurement of airflow velocities using an anemometer.

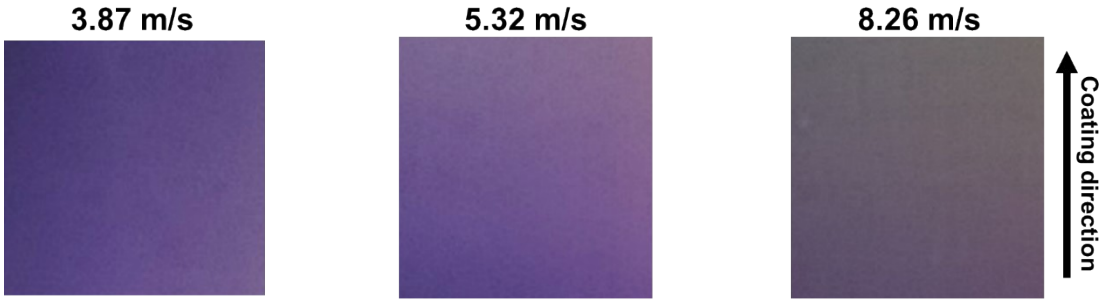

Fig. S6 Photographs of active layer films under different airflow velocities captured using a digital camera with macro-lens.

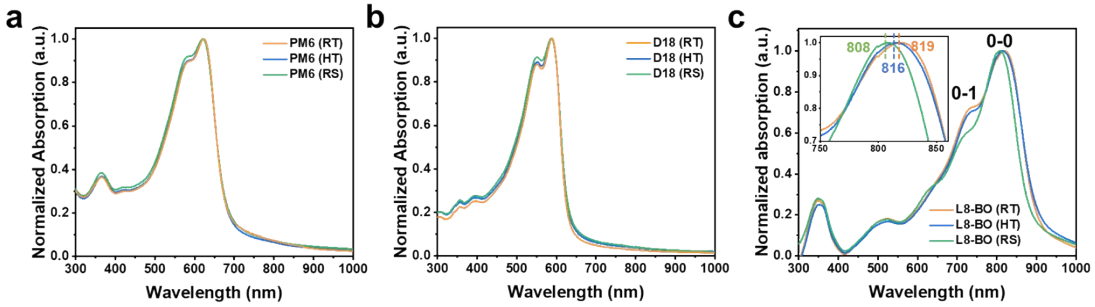

Fig. S7 Normalized UV-vis absorption spectra of **a)** PM6, **b)** D18, and **c)** L8-BO films fabricated using different processing methods.

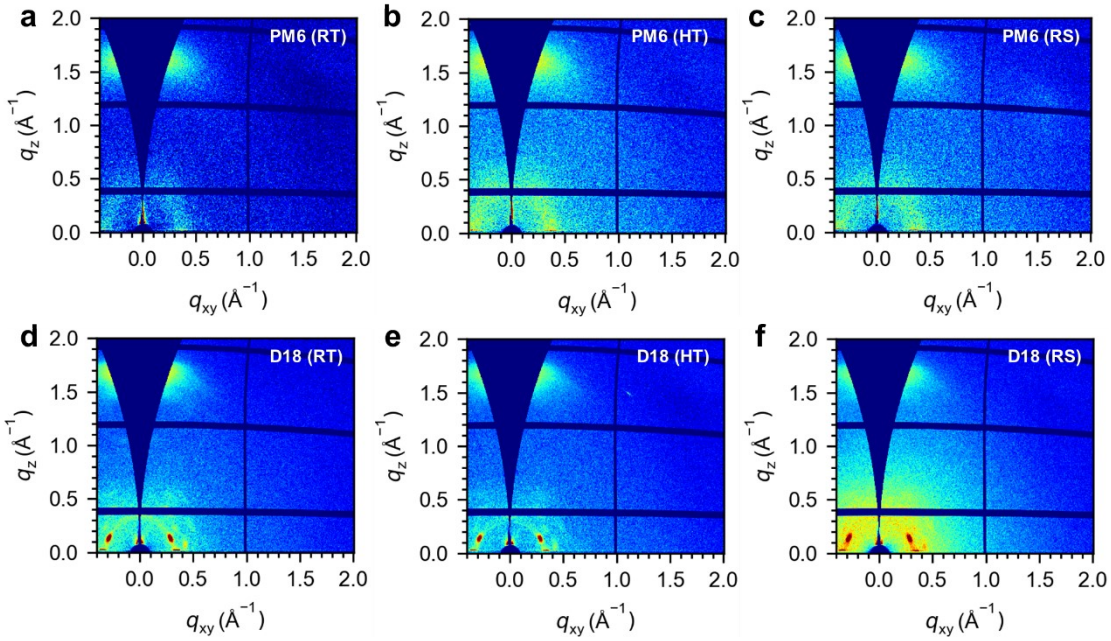

Fig. S8 2D GIWAXS patterns of the **a-c)** PM6 and **d-f)** D18 films fabricated using different processing methods.

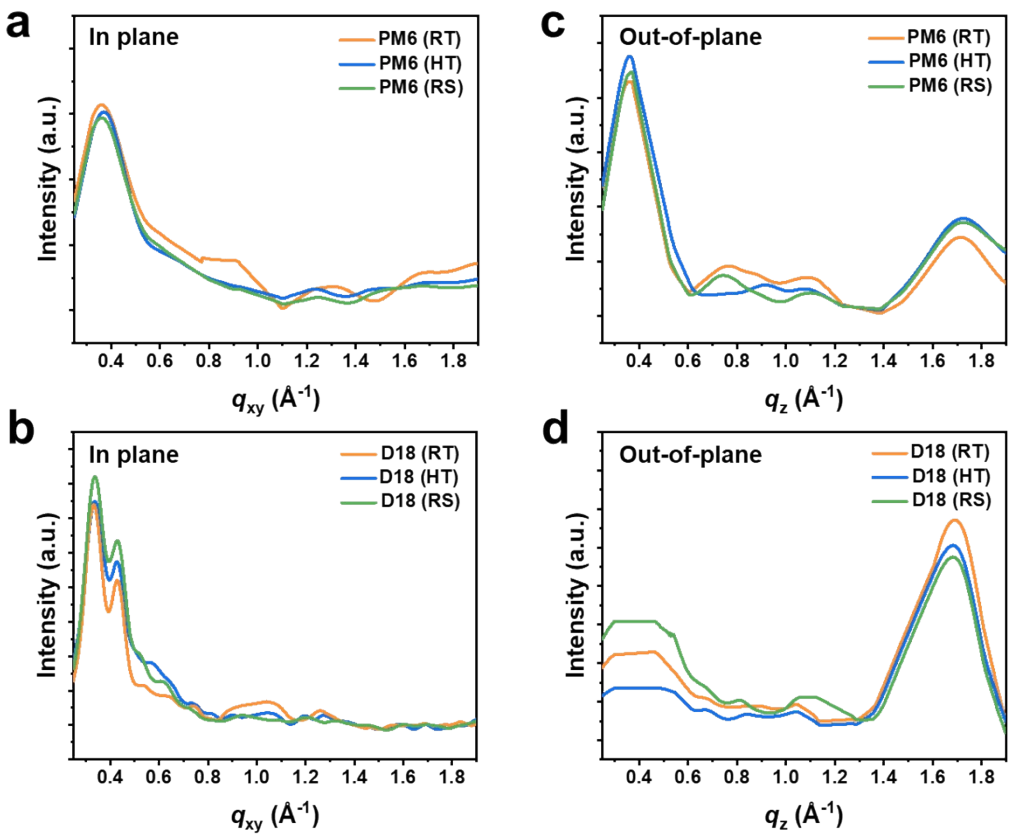

Fig. S9 Integrated scattering profiles for PM6 and D18 films, fabricated using different processing methods, along the **a-b)** IP and **c-d)** OOP directions.

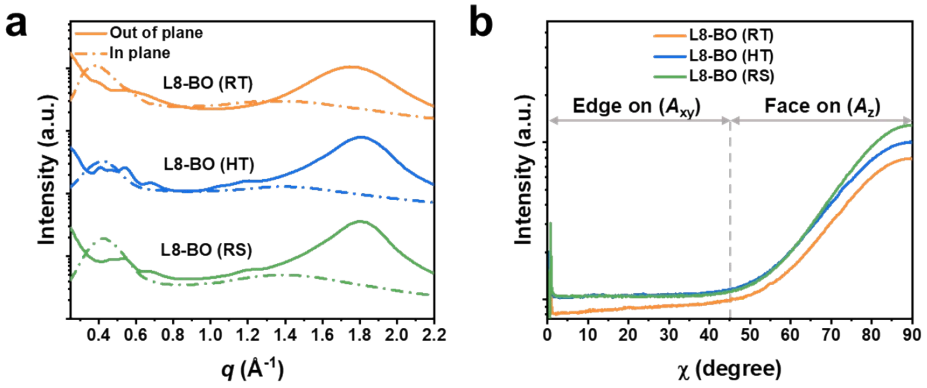

Fig. S10 a) Integrated scattering profiles for L8-BO films, fabricated using different processing methods, along the IP and OOP directions. **b)** Corresponding pole Fig.s extracted from the (010) diffraction patterns for L8-BO films.

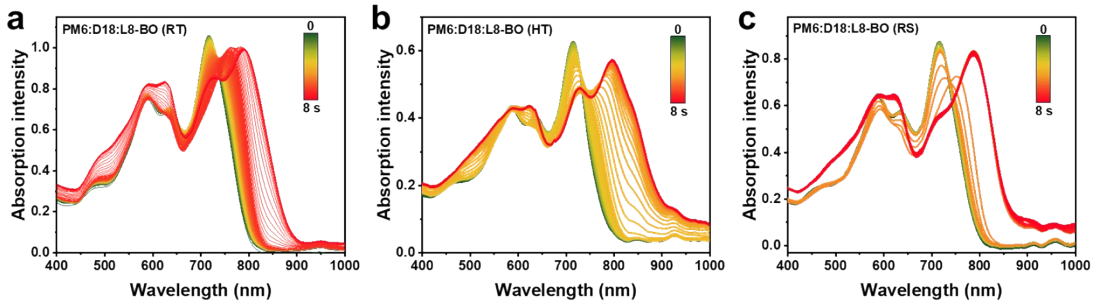

Fig. S11 *In-situ* UV-vis absorption of **a)** PM6:D18:L8-BO (RT), **b)** PM6:D18:L8-BO (HT) and **c)** PM6:D18:L8-BO (RS) evolution from the solution to the film.

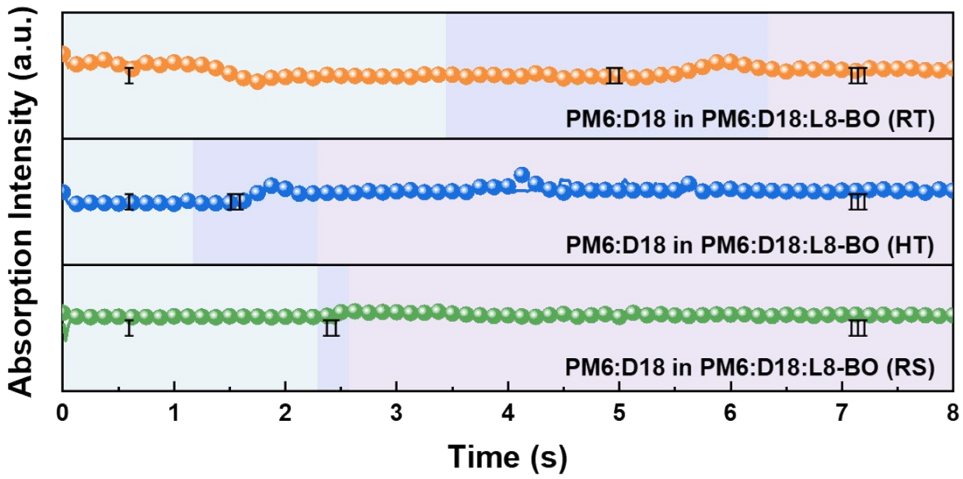

Fig. S12 Changes in the maximum absorption peak (~620 nm) intensity of PM6:D18 in PM6:D18:L8-BO.

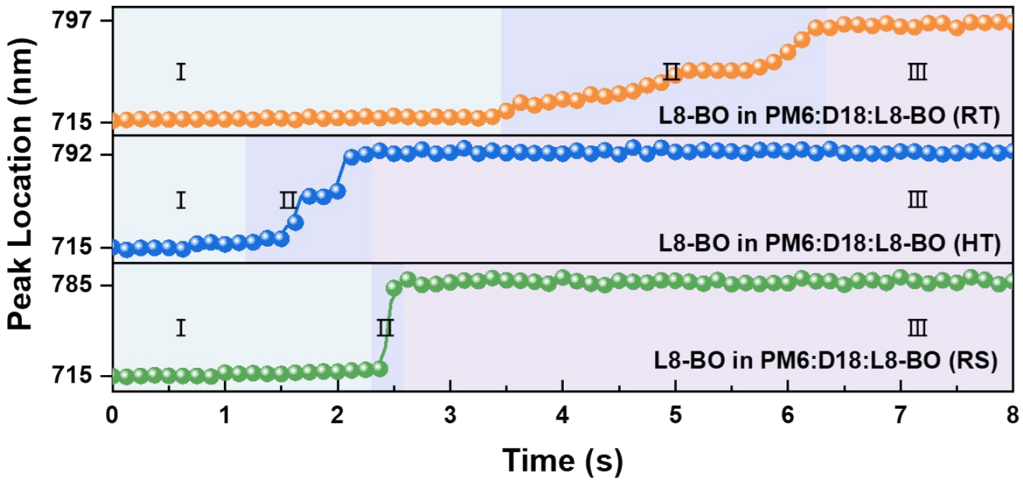

Fig. S13 Changes in the peak location (from 715 nm to ~790 nm) of L8-BO in PM6:D18:L8-BO fabricated using different processing methods.

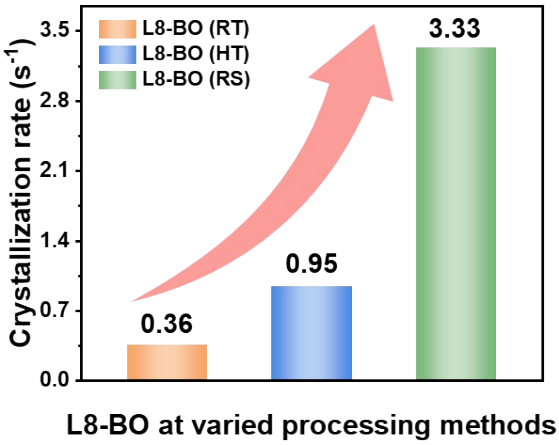

Fig. S14 Crystallization rate of L8-BO in PM6:D18:L8-BO fabricated using different processing methods.

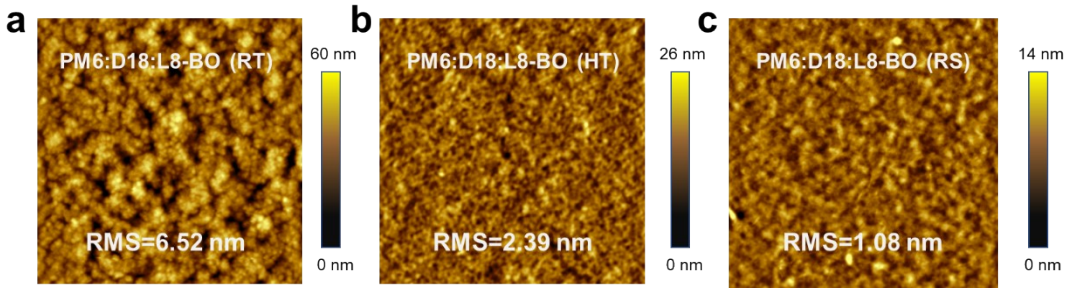

Fig. S15 AFM height images of PM6:D18:L8-BO active layer films (5×5 μm) fabricated using different processing methods.

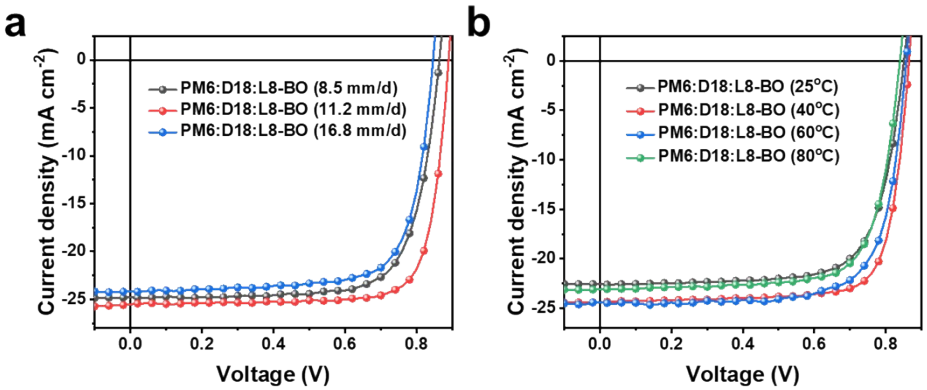

Fig. S16 *J*–*V* curves of PM6:D18:L8-BO at different **a)** evaporation rates and **b)** substrate temperatures under AM1.5G illumination with an intensity of 100 mW cm^{-2}.

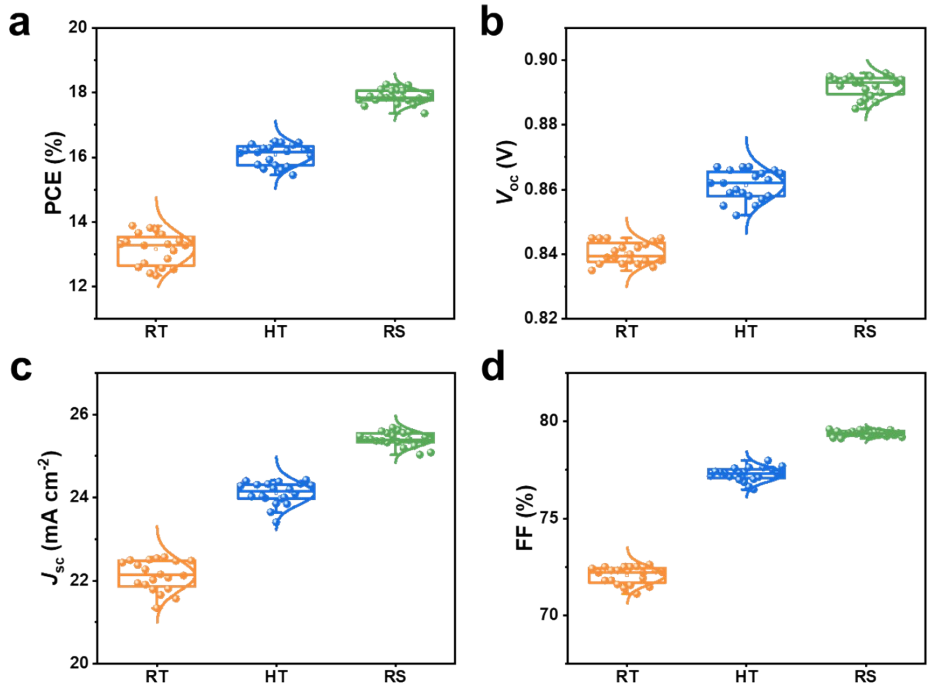

Fig. S17 Photovoltaic parameters statistics distribution of **a)** PCE, **b)** V_{oc}, **c)** J_{sc} and **d)** FF for the RT-, HT- and RS-based devices (20 individual devices were collected from the same batch).

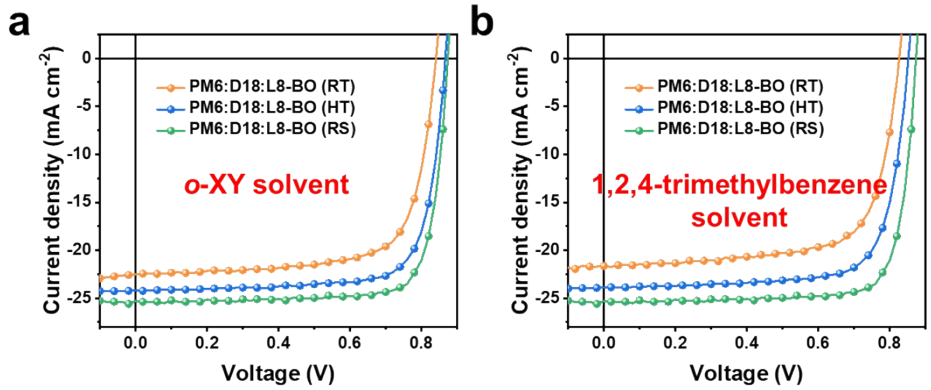

Fig. S18 *J*–*V* curves of **a)** PM6:D18:L8-BO (*o*-XY) and **b)** PM6:D18:L8-BO (1,2,4-trimethylbenzene) based OSCs, subjected to various processing methods, under AM1.5G illumination with an intensity of 100 mW cm^{-2}.

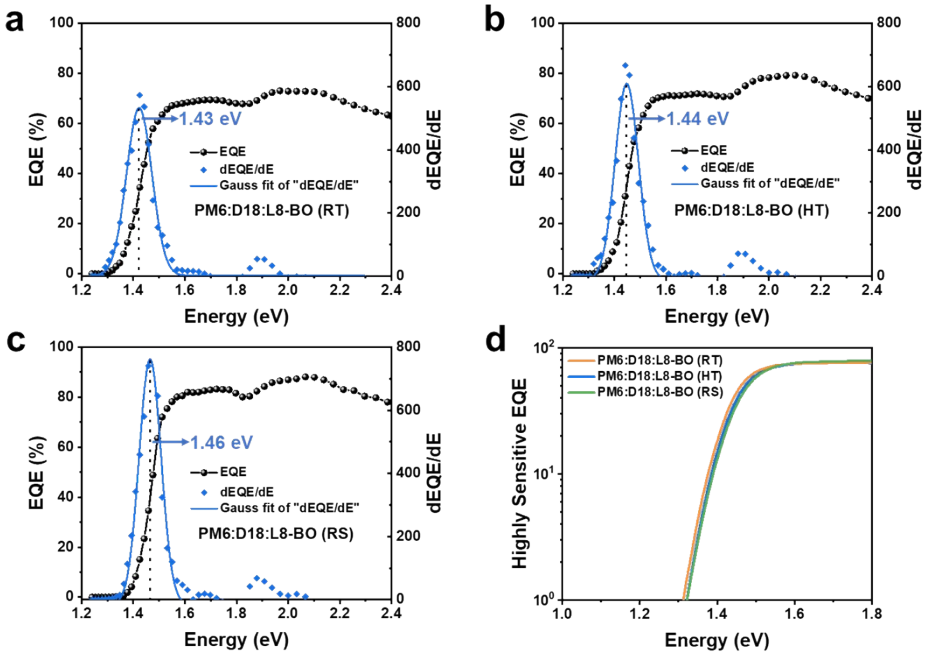

Fig. S19 Calculation of the optical bandgap of **a)** PM6:D18:L8-BO (RT), **b)** PM6:D18:L8-BO (HT) and **c)** PM6:D18:L8-BO (RS) by using the maximum point of the derivative of the EQE spectra (dEQE/dE). **d)** Highly sensitive EQE of PM6:D18:L8-BO-based OSCs subjected to various processing methods.

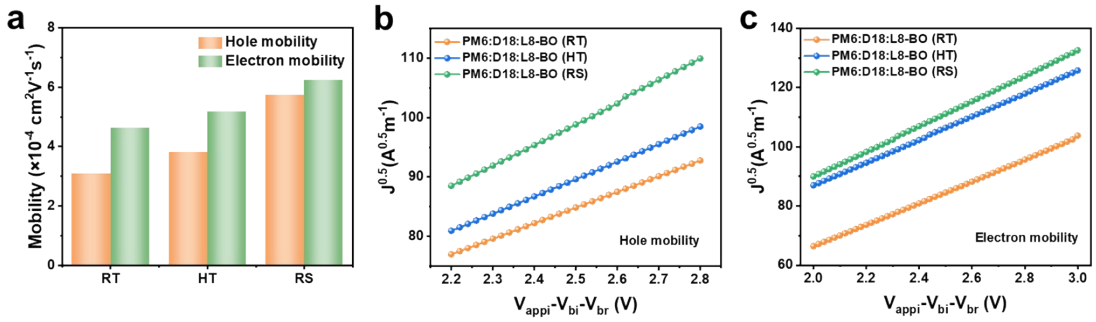

Fig. S20 a) Histogram of hole and electron mobilities for PM6:D18:L8-BO fabricated using different processing methods. **b-c)** Corresponding hole and electron mobility plots.

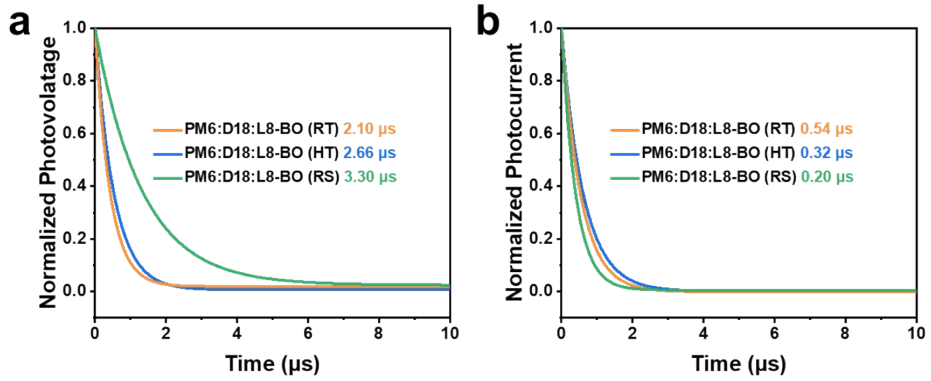

Fig. S21 a) TPV and **b)** TPC of PM6:D18:L8-BO fabricated using different processing methods.

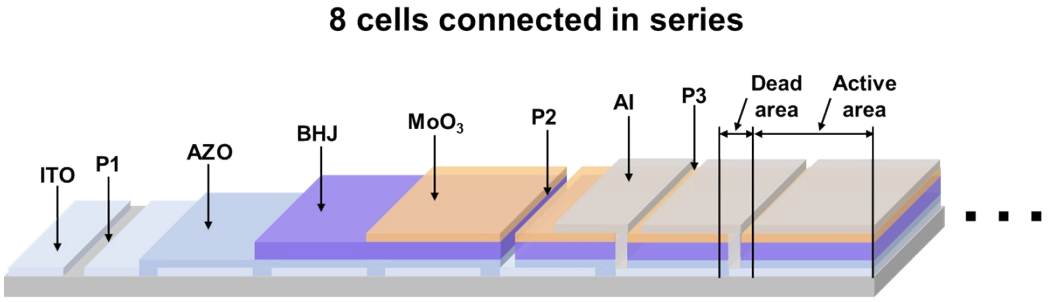

Fig. S22 Schematic illustration of the large-area module consisting of eight sub-cells (4.2×0.4655 cm^2) monolithically in series by ITO-to-Al interconnects.

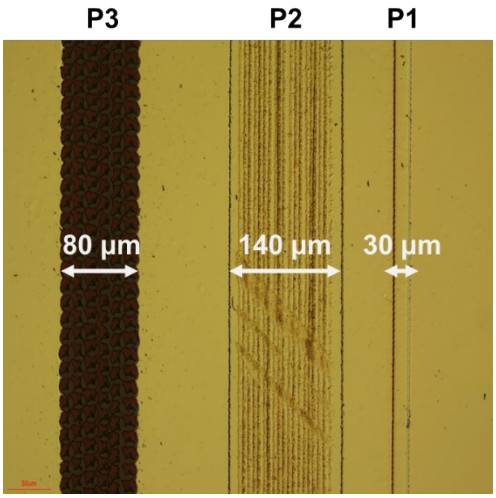

Fig. S23 Optical microscopic image of the P1, P2, and P3 etched lines for module fabrication. The width of P1, P2, and P3 is 30 μm, 140 μm, and 80 μm, respectively.

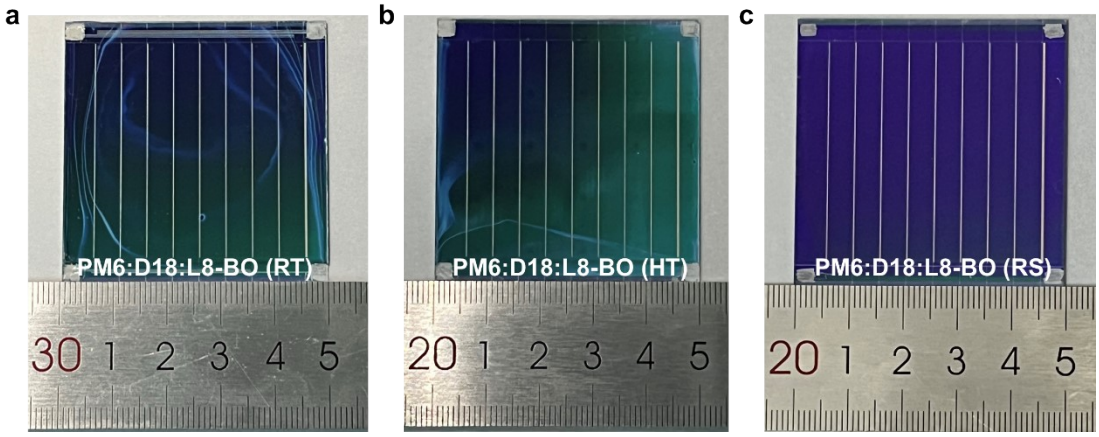

Fig. S24 The photograph of the blade-coated 15.64 cm^2 OSC modules subjected to various processing methods on 5×5 cm^2 substrate.

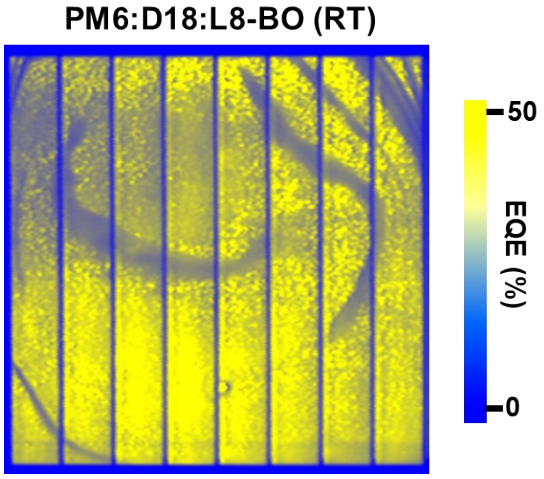

Fig. S25 The LBIC mapping image of the RT-based OSC module. The color scale bar represents the EQE intensity.

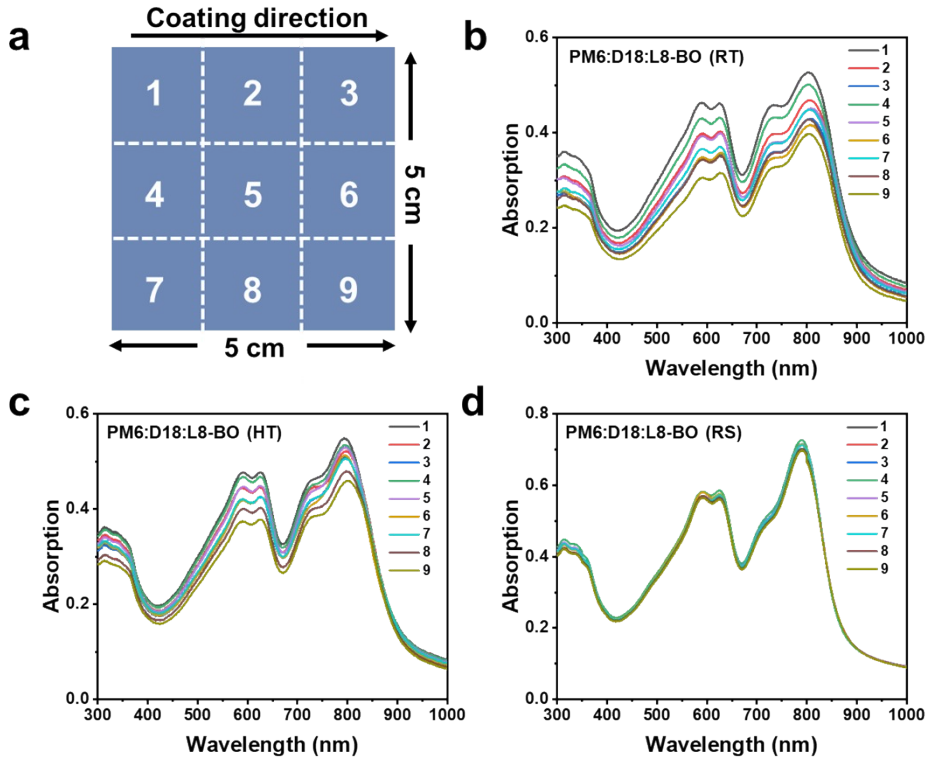

Fig. S26 a) Schematic illustration of nine platforms on a 5×5 cm^2 substrate. The UV-vis absorption spectra of nine platforms in **b)** PM6:D18:L8-BO (RT), **c)** PM6:D18:L8-BO (HT) and **d)** PM6:D18:L8-BO (RS) films, respectively.

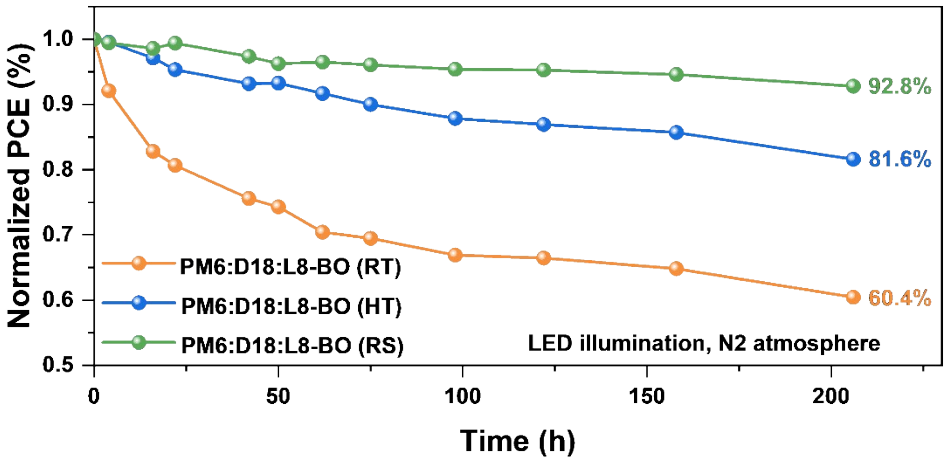

Fig. S27 The light stability of RT-, HT- and RS-based OSC modules in N_2 atmosphere under the illumination of a LED.

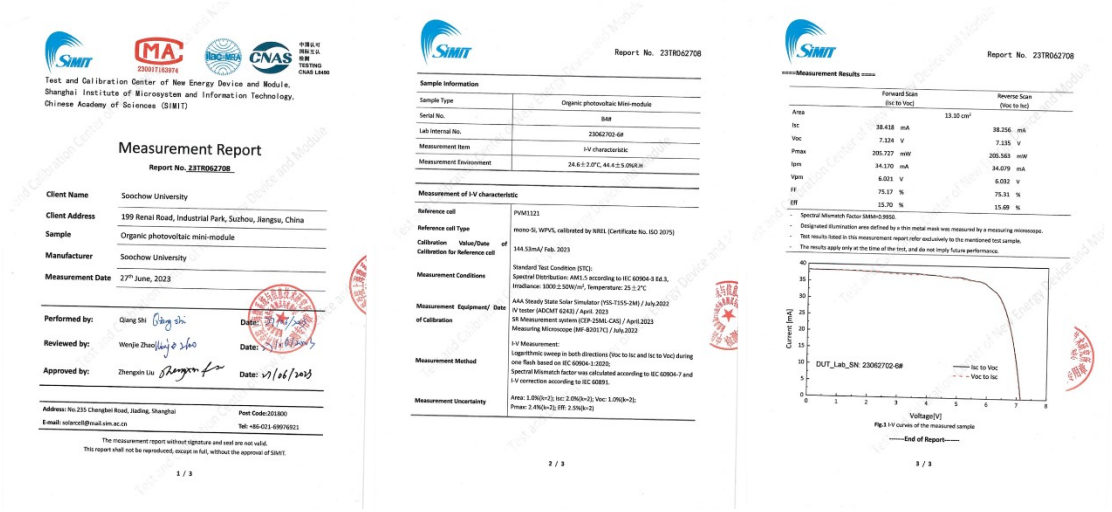

Fig. S28 Certification report for RS-based large-area module by SIMIT in Shanghai, China.

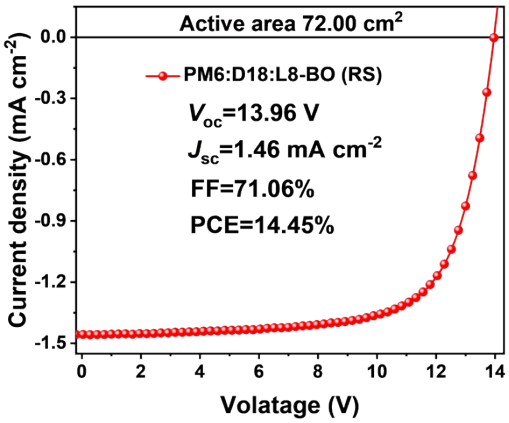

Fig. S29 *J–V* curve of the 72.00 cm^2 OSC module under AM1.5G illumination with an intensity of 100 mW cm^{-2}.

Table S1. Water and diiodomethane contact angles on the PM6:D18:L8-BO films at different substrate temperatures and the corresponding surface tension calculated with equations of state (Neumann).

Temperature (K)	Water contact angle (°)	Diiodomethane contact angle (°)	Surface tension γ (mN·m^{-1})	dγ/dT (mN·m^{-1}·k^{-1})
298	102.6	54.5	32.67	-0.059
313	104.6	55.9	32.15	
333	105.7	58.5	30.83	
353	107.0	60.5	29.51	

Table S2. The values of ΔT, L, μ, α, and $d\gamma/dT$ measured at different substrate temperatures.

ΔT[a] (K)	L (m)	μ (mPa·s)	α (m^2·s^{-1})	dγ/dT (mN·m^{-1}·k^{-1})	Marangoni number
0	9.8×10^{-5}	10.68	1.20×10^{-7}	-0.059	0
15		7.37	1.14×10^{-7}		103
35		4.52	1.06×10^{-7}		422
55		2.41	0.99×10^{-7}		1332

[a] The bottom temperature of the wet film is assumed to be the substrate temperature (as glass has high thermal conductivity), while the top temperature is room temperature (the solution temperature matches room temperature during coating).

Table S3. Calculation of evaporation rate at different airflow velocity.

Airflow velocity (m/s)	Evaporation rate (mm/d)
3.87	8.5
5.32	11.2
8.26	16.8

Table S4. The *d*-spacings and CCLs of IP (100) diffractions for PM6, D18 and L8-BO neat films fabricated using different processing methods.

Neat film	(100) Peak position (Å^{-1})	*d*-spacing (Å)	CCL (Å)
PM6 (RT)	0.35	18.15	46.71
PM6 (HT)	0.36	17.46	47.79
PM6 (RS)	0.34	18.32	51.47
D18 (RT)	0.34	18.80	70.71
D18 (HT)	0.33	18.96	72.00
D18 (RS)	0.34	18.81	69.17
L8-BO (RT)	0.39	16.19	30.92
L8-BO (HT)	0.42	14.99	34.09
L8-BO (RS)	0.43	14.72	43.53

Table S5. The *d*-spacings and CCLs of OOP (010) diffractions for PM6, D18 and L8-BO neat films fabricated using different processing methods.

Neat film	(010) Peak position (Å^{-1})	*d*-spacing (Å)	CCL (Å)
PM6 (RT)	1.69	3.73	24.48
PM6 (HT)	1.69	3.72	24.95
PM6 (RS)	1.68	3.73	25.06
D18 (RT)	1.67	3.77	40.81
D18 (HT)	1.67	3.76	41.22
D18 (RS)	1.67	3.76	42.36
L8-BO (RT)	1.76	3.57	22.45
L8-BO (HT)	1.80	3.50	27.54
L8-BO (RS)	1.80	3.49	29.37

Table S6. The ratio of face-on (A_z) and edge-on orientation (A_{xy}) for L8-BO neat films fabricated using different processing methods.

Neat film	A_z (%)	A_{xy} (%)	A_z/A_{xy}
L8-BO (RT)	79.75	20.25	3.94
L8-BO (HT)	80.76	19.24	4.20

L8-BO (RS)	83.27	16.73	4.98

Table S7. The *d*-spacings and CCLs of IP (100) diffractions for PM6:D18:L8-BO blend films fabricated using different processing methods.

Active layer	(100) Peak position (Å^{-1})	*d*-spacing (Å)	CCL (Å)
PM6:D18:L8-BO (RT)	0.31	19.88	34.71
PM6:D18:L8-BO (HT)	0.33	19.16	43.85
PM6:D18:L8-BO (RS)	0.33	18.93	57.73

Table S8. The *d*-spacings and CCLs of OOP (010) diffractions for PM6:D18:L8-BO blend films fabricated using different processing methods.

Active layer	(010) Peak position (Å^{-1})	*d*-spacing (Å)	CCL (Å)
PM6:D18:L8-BO (RT)	1.75	3.59	21.28
PM6:D18:L8-BO (HT)	1.77	3.55	24.05
PM6:D18:L8-BO (RS)	1.78	3.53	31.81

Table S9. The ratio of face-on (A_z) and edge-on orientation (A_{xy}) for PM6:D18:L8-BO blend films fabricated using different processing methods.

Active layer	A_z (%)	A_{xy} (%)	A_z/A_{xy}
PM6:D18:L8-BO (RT)	79.50	20.50	3.98
PM6:D18:L8-BO (HT)	80.41	19.59	4.10
PM6:D18:L8-BO (RS)	81.57	18.43	4.43

Table S10. Photovoltaic parameters of PM6:D18:L8-BO at different evaporation rates under AM1.5G 100 mW cm^{-2} illumination.

Evaporation rate (mm/d)	V_{oc} (V)	J_{sc} (mA cm^{-2})	FF (%)	PCE (%)
8.5	0.865	24.77	74.69	16.00

11.2	0.895	25.62	79.50	18.22
16.8	0.847	24.16	74.51	15.26

Table S11. Photovoltaic parameters of PM6:D18:L8-BO at different substrate temperatures under AM1.5G 100 mW cm^{-2} illumination.

Substrate temperature (°C)	V_{oc} (V)	J_{sc} (mA cm^{-2})	FF (%)	PCE (%)
25	0.845	22.54	72.50	13.82
40	0.867	24.43	77.97	16.50
60	0.857	24.44	74.07	15.52
80	0.833	22.98	74.81	14.59

Table S12. Photovoltaic parameters of PM6:D18:L8-BO (*o*-XY) based OSCs, subjected to various processing methods, under AM1.5G 100 mW cm^{-2} illumination.

Active layer	V_{oc} (V)	J_{sc} (mA cm^{-2})	FF (%)	PCE (%)
PM6:D18:L8-BO (RT)	0.840	22.68	71.60	13.64
PM6:D18:L8-BO (HT)	0.864	24.23	76.58	16.03
PM6:D18:L8-BO (RS)	0.871	25.42	79.78	17.65

Table S13. Photovoltaic parameters of PM6:D18:L8-BO (1,2,4-trimethylbenzene) based OSCs, subjected to various processing methods, under AM1.5G 100 mW cm^{-2} illumination.

Active layer	V_{oc} (V)	J_{sc} (mA cm^{-2})	FF (%)	PCE (%)
PM6:D18:L8-BO (RT)	0.824	21.70	70.62	12.63
PM6:D18:L8-BO (HT)	0.850	23.89	75.22	15.27
PM6:D18:L8-BO (RS)	0.869	24.99	79.10	17.17

Table S14. Statistical energy losses of PM6:D18:L8-BO fabricated using different processing methods.

Active layer	E_g (eV)	E_{loss} (eV)	EQE_{EL}	ΔE_1 (eV)	ΔE_2 (eV)	ΔE_3 (eV)
PM6:D18:L8-BO (RT)	1.43	0.585	1.8×10^{-5}	0.266	0.038	0.281
PM6:D18:L8-BO (HT)	1.44	0.573	3.7×10^{-5}	0.267	0.044	0.262
PM6:D18:L8-BO (RS)	1.45	0.555	7.2×10^{-5}	0.268	0.051	0.245

Table S15. The hole and electron mobilities for PM6:D18:L8-BO fabricated using different processing methods.

Active layer	Hole mobility (μ_h, $cm^2V^{-1}s^{-1}$)	Electron mobility (μ_e, $cm^2V^{-1}s^{-1}$)	μ_e/μ_h
PM6:D18:L8-BO (RT)	3.08×10^{-4}	4.64×10^{-4}	1.51
PM6:D18:L8-BO (HT)	3.80×10^{-4}	5.18×10^{-4}	1.36
PM6:D18:L8-BO (RS)	5.74×10^{-4}	6.23×10^{-4}	1.09

Table S16. The summary of PCEs of the green-solvent-processed large-area modules with active layer areas over 10 cm^2.

Area (cm^2)	PCE (%)	Active layer	Processing solvent	Ref.
16.5	13.84	PM6:PY-82:PY-DT	*o*-XY	S1. Adv. Mater. 2023, 35, 2208165
18	14.4	PM6:DTY6	*o*-XY	S2. Joule 2020, 4, 2004
18.73	14.79	PM6:BTP-BO-4Cl	PhMe	S3. Adv. Mater. 2022, 34, 2110569
20.4	10.13	TPD-3F:IT-4F	*o*-XY	S4. Joule 2020, 4, 189
21	15.4	D18:DTC11	Carbon disulfide and *o*-XY	S5. Adv. Energy Mater. 2023, 13, 2302273
25.2	14.42	PM6:CH7	*o*-XY	S6. Solar RRL 2023, 7, 2300029
25.21	14.07	PM6:BTP-eC9	PhMe	S7. Adv. Funct. Mater. 2022, 32, 2110209
28.82	12.64	PM6/Y6	*o*-XY	S8. J. Mater. Chem. C 2023, 11, 13263

30	12.2	PM6:Qx-1	*o*-XY	S9. Adv. Mater. 2023, 35, 2209030
31.5	12.44	PM6:Y6-hu	*o*-XY	S10. Adv. Energy Mater. 2023, 13, 2203452
36	14.26	PM6:Y6:BTO:$PC_{71}BM$	Paraxylene	S11. Nat. Energy 2021, 6, 1045
46.2	13.25	PM6:G-Trimer	*o*-XY	S12. Joule 2023, 7, 2386
54.45	11.6	PTF5:Y6-BO	*o*-XY	S13. Adv. Sci. 2023, 10, 2302376
55	13.88	PM6:P2:Y7-BO	*o*-XY	S14. Adv. Energy Mater. 2023, 13, 2302538
55.5	9.32	PTB7-Th:EH-IDTBR:T2-OEHRH	PhMe	S15. J. Mater. Chem. A 2020, 8, 10318
72.25	12.78	PM6:L8-BO: BTP-S8:BTP-S2	PhMe	S16. Chem. Eng. J. 2023, 473, 145201
15.64	**16.03**	**PM6:D18:L8-BO**	**PhMe**	**This work**
72.00	**14.45**	**PM6:D18:L8-BO**	**PhMe**	**This work**

References

1 M. R. Ahmadian-Yazdi and M. Eslamian, *Langmuir*, 2021, **37**, 2596-2606.

2 M. Sega, B. Fábián, G. Horvai and P. Jedlovszky, *J. Phys. Chem. C*, 2016, **120**, 27468-27477.

3 Y. Wang, D. Qian, Y. Cui, H. Zhang, J. Hou, K. Vandewal, T. Kirchartz and F. Gao, *Adv. Energy Mater.,* 2018, **8**. 1801352.